Phys Chem Minerals (2003) 30: 131–141
DOI 10.1007/s00269-003-0302-x

ORIGINAL PAPER

N. S. Lees · C. J. Walsby · J. A. S. Williams‡
J. A. Weil · R. F. C. Claridge

EPR of a hydrogen/double-lithium centre in α-quartz

Received: 12 June 2002 / Accepted: 10 January 2003

Abstract X-band electron paramagnetic resonance experiments on a gamma-irradiated α-quartz crystal have revealed a new hydrogarnet-like defect. Analysis of the spectral data suggests that the centre consists of an oxygenic electron hole adjacent to a silicon vacancy, charge-compensated by a proton and two lithium +1 ions. The principal directions of the spin-Hamiltonian *g* matrix indicate that the oxygenic hole occurs on the oxygen ion that would be long-bonded to the missing silicon atom. Modelling of the proton and lithium hyperfine matrices via three different methods has provided a detailed physical view for the structure of the defect centre, which is presented here.

Introduction

EPR studies of α-quartz have revealed a large number of paramagnetic ($S = 1/2$) oxygenic-hole species in both natural and synthetic crystals. Many of these centres, such as the neutral centre $[AlO_4]^0$ (Nuttall and Weil 1981a), the related charged centres $[AlO_4/H]^+$, $[AlO_4/Li]^+$ (Nuttall and Weil 1981b) and $[AlO_4/Na]^+$ (Dickson and Weil 1990), the recently reported $[AlO_4/Li]^q$ (here q is thought to be −1, Walsby et al. 2002), and also the triplet-state $S = 1$ centre $[AlO_4]^+$ (Nuttall and Weil 1981c), involve the replacement of a silicon atom by an aluminum atom. Another family of centres appears to involve the trapping of an oxygen hole next to a silicon vacancy, charge-compensated by sufficiently small +1 ions. The first examples of such centres, comprising an oxygen hole and a silicon vacancy associated with four and three protons, respectively, were reported by Nuttall and Weil (1980a). These two paramagnetic centres were designated $[H_4O_4]^+$ and $[H_3O_4]^0$. This family of hydrogenic centres is now thought to have considerable geochemical significance. The paramagnetic defect $[H_4O_4]^+$ is most likely formed from the neutral diamagnetic "hydrogarnet" defect[1] $[H_4O_4]^0$ by the loss of an electron. This latter defect has been postulated to be significant in the hydrolytic weakening of rock and is the subject of a number of publications. Purton et al. (1992) modelled the hydrogarnet defect in quartz using local density functional (LDF) pseudopotential calculations on a 36-atom cluster. This work was extended by Lin et al. (1994), who calculated the energy of formation of the hydrogarnet defect from interstitial water and found this process to be energetically favourable. Ab-initio calculations indicated that there is a substantial stress in the vicinity of the defect, and that this stress is likely to be minimized by the segregation of the defects into $10\bar{1}0$ planes. Lin et al. (1994) and McConnell et al. (1995) suggest that such segregation is the explanation for the crystallographically oriented lattice defects observed in the $(10\bar{1}0)$ planes by McLaren et al. (1983) using electron microscopy on reasonably wet[2] unheated crystals.

McConnell et al. (1995) used the calculations of Lin et al. (1994) to calculate the solubility in quartz of water in the form of the hydrogarnet defect as the temperature is varied under isobaric conditions. They concluded that the solubility has a maximum at a temperature which depends on the external water pressure, and then decreases as the temperature is raised further, in contrast to the earlier results of Paterson (1986). This leads to the conclusion that wet quartz on heating reacts to produce

N. S. Lees · C. J. Walsby · R. F. C. Claridge
Department of Chemistry, University of Canterbury,
Private Bag 4800, Christchurch, New Zealand

J. A. Weil (✉)
Department of Chemistry, University of Saskatchewan,
110 Science Place, Saskatoon, Saskatoon S7 N 5C9, Canada.
e-mail: john.weil@usask.ca

N. S. Lees · C. J. Walsby
Department of Chemistry, Northwestern University,
2145 Sheridan Road, Evanston, Illinois 60208-3113, USA

‡Deceased August 2001

[1]Also denoted, elsewhere, as $(4H)_{Si}$ and $(OH)_4$. This type of defect occurs in numerous nominally anhydrous materials (e.g., see Nobes et al. 2000)
[2]Quartz containing O–H bonds, as shown by IR spectroscopy

quartz and molecular water. The water bubbles thus produced lead to the nucleation of prismatic dislocation loops and promote dislocation climb (McLaren et al. 1983, 1989; Cordier and Doukhan 1989), resulting in hydrolytic weakening. As the reaction of the hydrogarnet defects to form quartz and water requires diffusion of the defects, their rate of diffusion may well be the rate-controlling process of the deformation of quartz in nature (Cordier et al. 1994).

A previously unreported paramagnetic centre designated $[HLi_2O_4]^0$, which most likely is related to this group of centres, has now been characterized by EPR. The charge compensation in this case is provided by one proton and two lithium +1 ions. Detailed EPR data for this centre are reported here and are compared with the hole-bearing aluminum and multihydrogen centres.

Experimental

The crystal studied is a synthetic α-quartz crystal grown hydrothermally by Sawyer Research Products, Inc. (Eastlake, Ohio). The growth run took place over 64 days within a stainless-steel autoclave which was not silver-lined. This led to the minor presence of some iron impurities in the crystal, as evidenced by observation of EPR signals from the $[FeO_4/H]^0_\alpha$ centre previously reported by Mombourquette et al. (1989). A rectangular parallelepiped of dimensions $4.27 \times 5.25 \times 5.02$ mm (labelled 191d) was cut from our plate 191 such that a pair of its faces was perpendicular to the threefold optical axis ($\boldsymbol{c}$) and another pair was perpendicular to one ($\boldsymbol{a}_1$) of the three twofold crystal axes. This plate was gamma-irradiated at room temperature using a ^{60}Co source for 18 h with a dose rate of 2687 rad min^{-1}, more than a month prior to the first EPR measurements.

The crystal plate was mounted in a cavity goniometer system described previously by Claridge et al. 1994. The x axis of the Cartesian axis system fixed in the crystal was chosen to be $\boldsymbol{a}_1$ and was aligned parallel to $\boldsymbol{B}_\mu$, the microwave excitation magnetic field. Rotation about this axis allowed EPR measurements with the applied Zeeman magnetic field $\boldsymbol{B}$ in the perpendicular plane (yz). At arbitrary orientations of $\boldsymbol{B}$, spectra from the six symmetry-related sites are visible, but collapse to three doubly degenerate spectra when $\boldsymbol{B}$ is perpendicular to $\boldsymbol{a}_1$, and to one spectrum when $\boldsymbol{B}$ is parallel to $\boldsymbol{c}$ (chosen as the z axis in the Cartesian crystal axis system). The axis system and definition of the polar angle θ and azimuthal angle ϕ via which the EPR results are reported are identical to those described in detail by Nuttall and Weil (1981a).

The collapse of the six spectra from the symmetry-related sites to three spectra for $\boldsymbol{B}$ in the plane of measurement allowed accurate and precise alignment of the crystal in this plane. A screwdriver setup (Perlson and Weil 1975) allowed adjustment while the crystal was inside the EPR cavity. Adjustments were carried out while observing an oscilloscope trace of the $[AlO_4]^0$ EPR signal until all pairs of lines collapsed, each to a single line, at any orientation of $\boldsymbol{B}$ within the rotation plane. The narrow linewidths (ca. 0.01 mT) thus allowed alignment in the plane with an accuracy of ca. 5′.

Measurements were made at ca. 100 K. At lower temperatures, the $[AlO_4]^0$ EPR spectrum is very intense and obscures the $[HLi_2O_4]^0$ spectrum. Data were collected using a computer-interfaced Varian E12 spectrometer, with a Varian E-101 X-band microwave bridge as the microwave source. The microwave frequency typically was ca. 9.28 GHz (accurate to ± 10 kHz). Spectra were recorded at 5° intervals over 180° (± 1′ uncertainty), with all three pairs of sites measurable within a 10 mT scan range (field precision ± 0.001 mT). The data taken in the yz plane were sufficient to determine the major spin-Hamiltonian parameter matrices (Weil et al. 1973). In order to show that the stated levels of precision were not too high to produce meaningful results, the data set was fitted with a precision level limit of 100 kHz and also of 10 kHz in frequency, as well as 0.001 mT and 0.01 mT in the magnetic field. This had no effect on either the output matrices or the subsequent analysis. The appropriate spin-Hamiltonian operator for the analysis of this system with a single unpaired electron was taken (for any one of the six sites) to be:

$$\hat{H}_s = \beta_e \boldsymbol{B}.\boldsymbol{g}.\hat{\boldsymbol{S}} + \sum_i (\hat{\boldsymbol{I}}_i.\boldsymbol{A}_i.\hat{\boldsymbol{S}} + \hat{\boldsymbol{I}}_i.\boldsymbol{P}_i.\hat{\boldsymbol{I}}_i - \beta_n \boldsymbol{B}.\boldsymbol{g}_{ni}.\hat{\boldsymbol{I}}_i) \quad , \tag{1}$$

where the subscript i refers to the three nuclear spin $I \neq 0$ nuclei involved in the centre. Quantum-mechanical operators are indicated by carets. The nuclear Zeeman-splitting factors g_n were assumed to be isotropic ($\boldsymbol{g}_{ni} = g_{ni}\ \boldsymbol{U}$, where $\boldsymbol{U}$ is the 3×3 unit matrix), and were taken from appropriate tables (Weil et al. 1994, Table G.4). Matrices $\boldsymbol{g}$, $\boldsymbol{P}_i$ and $\boldsymbol{A}_i$ were fitted as being symmetric.

Effective hyperfine splittings for the three high-abundance $I \neq 0$ nuclei present were estimated, over the range of measured angles, by attempting to simulate the primary lines in the observed spectra. This was achieved using the software program WIN-EPR SimFonia (Weber 1995) which simulates EPR spectra by calculating line positions using perturbation energies (Abragam and Bleaney 1970; Weil 1975) when hyperfine couplings for specific nuclei are specified, along with appropriate linewidths and lineshapes. These parameters were adjusted manually until each resultant spectrum best resembled the corresponding experimental spectrum. The splittings were then used to create an artificial set of line-position data for each nucleus individually, built upon an isotropic line position corresponding to $g = 2$. These data sets were entered into the program EPR-NMR (Mombourquette et al. 1996) and the hyperfine matrices were then fitted. All of the hyperfine matrices were then used (together with a matrix $\boldsymbol{g}$ fitted from the central line positions) to simulate, using EPR-NMR, the spectra collected in the yz plane. This allowed the observed EPR lines to be assigned the correct pairs of transition (energy-level) labels by comparison with the simulations, a task which would otherwise have been very difficult. For this system with an electron spin $S = 1/2$, one $I = 1/2$ nucleus and two $I = 3/2$ nuclei, there are 1024 EPR transitions per site, at each field orientation. These arise from a 32-level energy manifold in each of the two electronic spin states occurring for $S = 1/2$, non-degenerate when an external magnetic field is present. However, EPR-NMR intensity calculations indicated that at least 90% of these transitions were too weak to be observed at most orientations. The line positions that were observed were entered and refitted until all measurable lines were included in the fitting procedure. The final EPR-NMR spectral simulations demonstrated an excellent reproduction of the measured spectra in both line positions and relative intensities for all three sites at all orientations explored.

Results

The EPR lines for centre $[HLi_2O_4]^0$ were found to remain narrow (peak-to-peak first-derivative linewidths 0.01–0.02 mT) up to ca. 100 K, the temperature at which measurements were made. Above 100 K, the sets of previously well-resolved quartet lines arising from the 92.5% abundant ^{7}Li nuclei began to broaden and merge.

The final fitting of the 100 K data contained 1886 line-position data points taken for the three doubly degenerate spectra over 37 crystal orientations, with $\boldsymbol{B}$ in the yz plane. The root-mean-squared deviation (RMSD) between the experimental and matrix-fitted line positions was 0.0035 mT, i.e., about 1/5 of the linewidth. A comparison between the experimental and simulated spectra for the orientation $\boldsymbol{B} \parallel \boldsymbol{c}$ can be seen in Fig. 1.

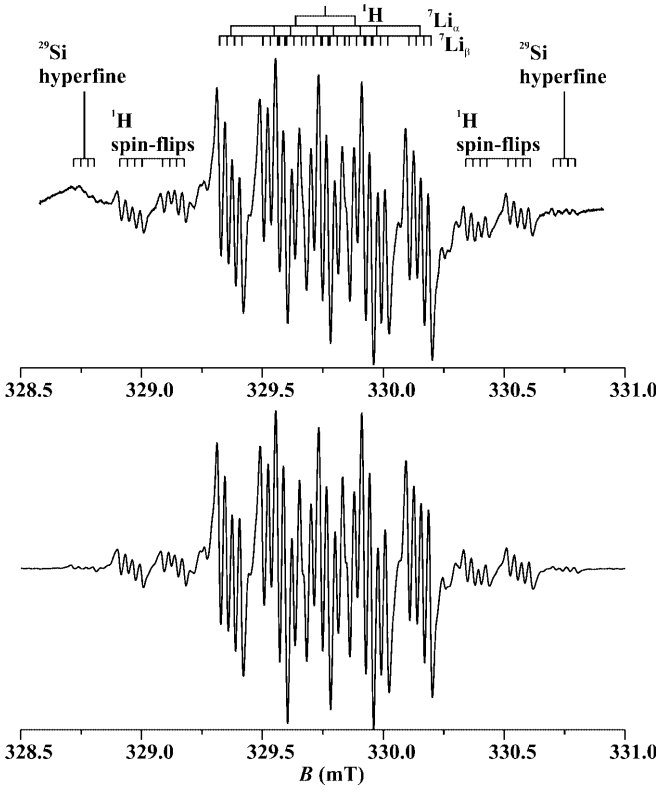

Fig. 1 Experimental (*top*) and simulated (*below*) EPR spectrum of centre $[HLi_2O_4]^0$ in α-quartz at ca. 100 K with $\boldsymbol{B} \parallel \boldsymbol{c}$. Frequency = 9.28188 GHz. The effective hyperfine splitting due to each high-abundance hyperfine nucleus is shown above the experimental spectrum. The broad lines *visible in the experimental spectrum* are due to $[AlO_4]^0$

All possible EPR transitions were included in the simulations, including the "spin-flip" transitions (Weil and Anderson 1961) involving a simultaneous change in electronic and nuclear-spin-component quantum numbers. Several of the proton spin-flip lines can clearly be seen (as quartets) with lower intensity, on the outside of the main lines as indicated in Fig. 1 (the clear fourfold splitting is due to hyperfine interaction with one (Li_β) of the ^{7}Li nuclei ($I = 3/2$). The positions of these lines depend on g_n, and are diagnostic of the nucleus present. The lithium spin flips are calculated to be lower in intensity than the proton spin flips, and occur closer to the centre of the spectrum. They cannot be seen as distinct lines, but their contribution to the lineshape is accurately reproduced in the simulation, confirming the identity of the hyperfine nuclei. The simulated spectrum includes contributions from several combinations of nuclear isotopes. The major contribution comes from (^{1}H, $^7Li_\alpha$, $^7Li_\beta$), but the spectra due to (^{1}H, $^7Li_\alpha$, $^6Li_\beta$), (^{1}H, $^6Li_\alpha$, $^7Li_\beta$), (^{1}H, $^6Li_\alpha$, $^6Li_\beta$) and (^{29}Si, ^{1}H, $^7Li_\alpha$, $^7Li_\beta$) were also included, with appropriate intensity ratios. The natural abundances of ^{6}Li and ^{29}Si are 7.5 and 4.7%, respectively. Contributions from other combinations with four hyperfine nuclei were not included because such simulations are time-consuming, and were judged to make no appreciable contribution to the spectrum due to their very low concentration. The (^{29}Si, ^{1}H, $^7Li_\alpha$, $^7Li_\beta$) spectrum, due to the hyperfine interaction arising from the low-abundance ^{29}Si, causes the set of lines visible on the extreme edges of the spectrum. However, the data collected were insufficient to fit ^{29}Si hyperfine matrices, due to the low intensity of the spectra at many angles.

The fitted spin-Hamiltonian parameter matrices ($\boldsymbol{Y}$) are given in Table 1. The hyperfine matrix signs are those which give the most sensible positions for the hyperfine nuclei, as discussed later. This set of matrices corresponds to site 1 of the three sites, acting as doubly degenerate in the *yz* plane. Site 1 is the "unique" site, which has a "roadmap" most distinct from the other two, as observed by the angular dependence of the three sites in the measured plane (see Fig. 2). It is the site associated with the rotation (x) axis, the other sites being associated with the remaining twofold axes, $\boldsymbol{a}_2$ and $\boldsymbol{a}_3$. Site 1 was distinguished from its (degenerate) partner site 1' by comparison of the g-matrix principal directions with those of the aluminum hole centres, for which site 1 had been chosen respectively to correspond to the hole on O_2 (short-bonded) or O_3 (long-bonded), rather than the sites O_1 or O_4 equivalent to these (as labelled in Fig. 4). The principal directions were found to correspond best with those of the long-bonded $[AlO_4]^0$ (Nuttall and Weil 1981a), as discussed below. The matrices associated with the other sites are given by the similarity transformations $\boldsymbol{R}_j.\boldsymbol{Y}.\boldsymbol{R}_j^{-1}$, where ($j = 1,...6$) is any of the six proper rotation matrices for the proper rotation group D_3 (Weil et al. 1973).

An attempt to fit nuclear quadrupole matrices $\boldsymbol{P}$ for the lithium nuclei produced matrix elements which were smaller than, or very close to, their error estimates. The RMSD was not significantly reduced, implying that quadrupole effects for this centre are too small to be obtainable from the present experiments.

Discussion

The assignment of the current centre as an oxygen-hole/silicon vacancy was made for two primary reasons. The oxygenic hole is indicated by a correlation which can be made between the principal directions of the g-matrix for this centre and that of a number of the known oxygenic-hole centres in quartz, including the well-known aluminum centres $[AlO_4]^0$, $[AlO_4/H]^+$, $[AlO_4/Li]^+$ and $[AlO_4/Na]^+$, as well as the hydrogenic silicon vacancy centres, $[H_4O_4]^+$ and $[H_3O_4]^0$. These centres all appear to be interrelated by rotations around the *c* axis, as can be seen in Table 2, and as is discussed below. The centres $[AlO_4/M]^+$, where $M = H^+$, Li^+, Na^+ all have similar principal directions and thus only $M = H^+$ is included in Table 2. Presence of a silicon vacancy is suggested by the resemblance to the $3H^+$ hole centre $[H_3O_4]^0$, the EPR spectrum of which is visible in the same crystal. Both centres contain three +1 charge-compensating ions and have similar g anisotropy. The presence of $[H_3O_4]^0$ shows that, on the assumption that

Table 1 Parameter matrices for centre $[HLi_2O_4]^0$ for site 1 in right α-quartz at 100 K[a]

	Matrix $\boldsymbol{Y}$			k	Principal value Y_k	Principal direction[b]	
						θ_k (°)	ϕ_k (°)
	2.009839(2)	0.008334(2)	−0.000650(1)	1	2.034377(2)	115.05(0)	70.57(0)
$\boldsymbol{g}$		2.025822(2)	−0.011332(1)	2	2.009657(2)	128.37(0)	182.28(0)
			2.0110472(8)	3	2.002674(1)	131.29(0)	316.33(0)
	−0.2177(6)	−0.1459(5)	0.1299(4)	1	0.5619(5)	142.1(1)	112.8(2)
$A_{1H}/g_e\beta_e$		−0.0027(6)	−0.3608(4)	2	−0.2145(5)	55.7(2)	141.3(4)
(mT)			0.2643(3)	3	−0.3035(5)	104.0(2)	221.5(3)
	0.0383(3)	0.0549(3)	0.0242(2)	1	−0.2437(2)	118.37(8)	98.4(3)
$A_{7Li\alpha}/g_e\beta_e$		−0.2148(3)	0.0379(2)	2	−0.1676(2)	29.60(6)	116.5(3)
(mT)			−0.1807(1)	3	0.0540(2)	97.7(1)	192.6(2)
	−0.0408(3)	0.0210(2)	−0.0368(2)	1	−0.0752(2)	136.5(3)	195.9(3)
$A_{7Li\beta}/g_e\beta_e$		0.0045(3)	−0.0399(2)	2	−0.0395(2)	66.3(3)	133.5(3)
(mT)			−0.0313(1)	3	0.0472(3)	56.0(2)	240.7(2)

[a] Error estimates in parentheses
[b] Note that set θ_k, ϕ_k is equivalent to set $180° - \theta_k$, $180° + \phi_k$. For our purposes, the sense of each direction is not meaningful

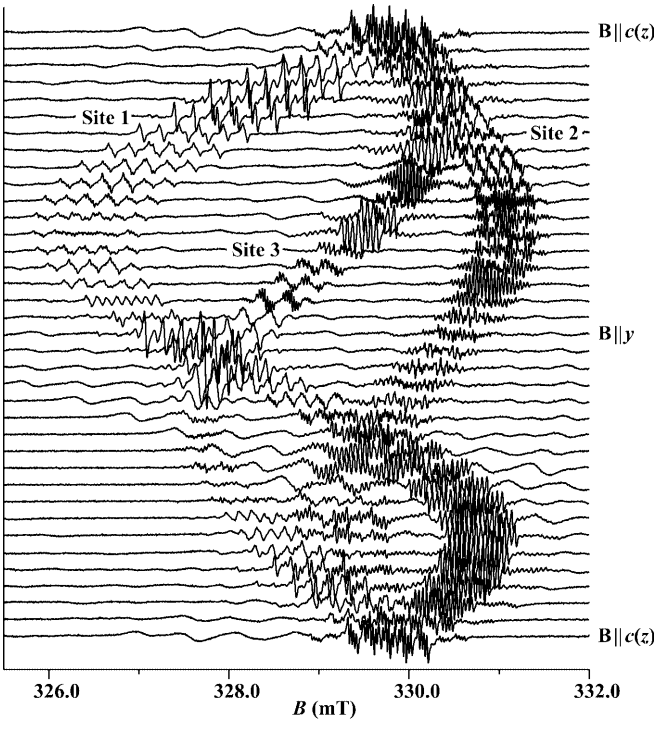

Fig. 2 Stacked plot for the $[HLi_2O_4]^0$ centre in α-quartz at ca. 100 K with $\boldsymbol{B}$ in the yz plane. Frequency ≈ 9.2832 GHz

the current accepted model for this centre is correct, silicon vacancies are indeed present. However, the $[HLi_2O_4]^0$ model still poses some unanswered questions which will be discussed below.

The α-quartz structure has two types of linkages between the oxygen and silicon ions: short bonds and long bonds. The difference in bond length is approximately 0.3%. For the previously referenced aluminum centres, the identity of the oxygen on which the hole is formed with respect to the aluminum site (substituted silicon site) has been established by comparison of the fitted spin-Hamiltonian parameter-matrix principal directions with directions in quartz associated which each oxygen position. Originally, the comparisons were made using x-ray crystallographic positions of pure quartz (Wyckoff 1963), later corroborated with positions provided by structural studies using MO calculations of the distorted lattice surrounding the impurities (Mombourquette et al. 1984; Mombourquette and Weil 1985). These analyses strongly support the conclusion that, in the case of the $[AlO_4]^0$ centre, the hole is located on a long-bonded oxygen, and in the centres $[AlO_4/H]^+$ and $[AlO_4/Li]^+$, located on a short-bonded oxygen. If the $[HLi_2O_4]^0$ centre is indeed an oxygenic hole centre, one must distinguish between the two types of oxygen ions adjacent to the silicon vacancy. While the presence of such a silicon vacancy would be expected to cause a distortion of the atom positions surrounding the vacancy from the normal lattice positions, it is likely that the significant difference between O_2 and O_3 of Fig. 3 (short- and long-bonded, respectively, in the perfect α-quartz structure) would remain, due to the constraints of the surrounding lattice. The principal directions of the g matrix of $[HLi_2O_4]^0$ would then be expected to bear a resemblance to those of $[AlO_4/H]^+$ and $[AlO_4/Li]^+$ (oxygen hole on O_2) or of $[AlO_4]^0$ (oxygen hole on O_3). This is indeed found to be the case, as shown in Table 2. The $[HLi_2O_4]^0$ g-matrix principal directions are much closer to those of $[AlO_4]^0$, while the $[H_4O_4]^+$ and $[H_3O_4]^0$ g-matrix principal directions are much closer to the $[AlO_4/H]^+$ and $[AlO_4/Li]^+$ directions. This implies that the oxygen hole is located on O_3 for $[HLi_2O_4]^0$, and O_2 for $[H_4O_4]^+$ and $[H_3O_4]^0$.

Furthermore, inspection of the directions presented in Table 2 in fact show that all of the θ angles are very similar, while the ϕ values increase by a roughly constant amount from centre to centre, as listed. This represents a rotation of the principal axis set about the z axis, by approximately 10° from $[AlO_4]^0$ to $[HLi_2O_4]^0$, and by approximately 20° from $[H_4O_4]^+$ and $[H_3O_4]^0$ to $[AlO_4/H]^+$ and $[AlO_4/Li]^+$. This may suggest that the silicon vacancy allows the dangling Si–O bond pointing

Table 2 Site-1 *g*-matrix principal directions [a] for the centres $[AlO_4]^0$, $[HLi_2O_4]^0$, $[H_3O_4]^0$, $[H_4O_4]^+$ and $[AlO_4/H]^+$ [b], given in order of rotation about the *z* axis

k	$[AlO_4]^0$		$[HLi_2O_4]^0$		$[H_3O_4]^0$		$[H_4O_4]^+$		$[AlO_4/H]^+$	
	θ_k (°)	ϕ_k (°)	θ_k (°)	ϕ_k (°)	θ_k (°)	ϕ_k (°)	θ_k (°)	ϕ_k (°)	θ_k (°)	ϕ_k (°)
1	119.25	57.62	115.05	70.57	119.54	141.99	124.18	146.18	120.13	167.70
2	124.43	305.05	131.29	316.33	123.23	30.20	124.46	28.41	127.62	51.14
3	131.65	177.49	128.37	182.28	132.52	263.29	127.13	267.12	127.79	284.44

[a] Note that set θ_k, ϕ_k is equivalent to set $180° - \theta_k$, $180° + \phi_k$. For our purposes, the sense of each direction is not meaningful
[b] $[AlO_4]^0$, $[AlO_4/H]^+$, measured at ca. 35 K, $[H_3O_4]^0$ and $[H_4O_4]^+$ at ca. 30 K, $[HLi_2O_4]^0$ at ca. 100 K

into the vacancy to rotate slightly towards the main *c*-axis channel, as shown in Fig. 3, with the silicon position and the angle between the *z*-axis and Si–O directions relatively unchanged.

Identification of the oxygen anion on which the hole is located enables the compensator-ion positions to be estimated, using the measured hyperfine interaction between the oxygenic electronic magnetic moment and the nuclear magnetic moments of the compensating ions. It should be noted that the analysis which follows assumes the atomic positions of the perfect crystal lattice to be unchanged. The *g*-matrix principal directions discussed above suggest that the true structure is not far removed from this case.

The positions of the compensator cations in the aluminum centres were initially estimated using a magnetic point-dipole–point-dipole approximation (Nuttall and Weil 1981b). Under this approximation, the hyperfine interaction matrix was taken to be uniaxial, and the distance between the oxygen ion and compensator M (= H^+, Li^+ or Na^+) was calculated from the magnitude of the dipolar component of the hyperfine matrix. The interatomic direction was assumed to be the unique principal direction of the hyperfine matrix. For a discussion of the various approximations made and possible errors existing, see Appendix A in Mombourquette et al. (1995).

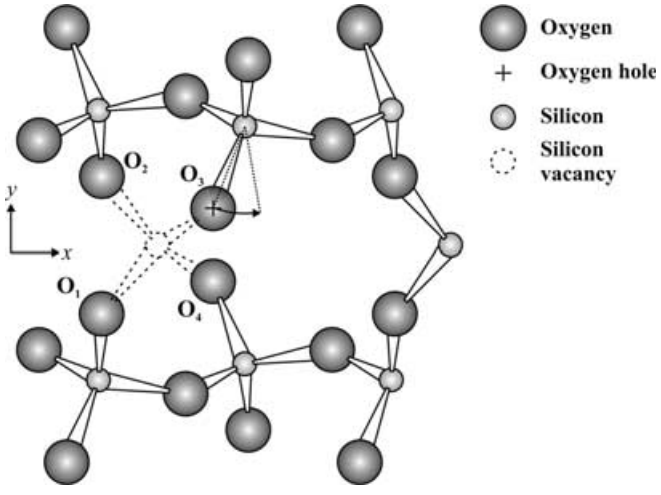

Fig. 3 Rotation of the Si–O dangling bond about the silicon atom, towards the nearest main *c*-axis channel, as suggested by the g-matrix principal directions. The degree of rotation is here exaggerated for clarity

The uniaxiality approximation is not completely appropriate for $[HLi_2O_4]^0$, since the hyperfine matrices are more rhombic than those of the aluminum centres $[AlO_4/H]^+$ and $[AlO_4/Li]^+$ (Nuttall and Weil 1981b). The rhombic component is significant for the lithium hyperfine matrices, while the proton hyperfine matrix is approximately uniaxial. The isotropic, uniaxial and rhombic hyperfine parameters *a*, *b*, *c* (Weil et al. 1994, p.116) calculated using the matrix signs as in Table 1, are given in Table 3 for the three hyperfine nuclei of $[HLi_2O_4]^0$. Nevertheless, the point-dipole–point-dipole approach was used as a first approximation for calculating all three compensator positions.

The distance *R* between the oxygenic hole and the hyperfine nucleus M was estimated from the dipolar hyperfine matrix $\boldsymbol{T}$ using the relation:

$$\frac{\boldsymbol{T}}{g_e\beta_e} = \frac{\mu_0}{4\pi} g_n \beta_n R^{-3} |c_x|^2 \begin{pmatrix} 2 & 0 & 0 \\ & -1 & 0 \\ & & -1 \end{pmatrix} , \qquad (2)$$

where $|c_x|^2$ is the absolute magnitude squared of the coefficient of the orbital labelled $x = nl$ in the unpaired-

Table 3 Principal values of the anisotropic parts of the centre $[HLi_2O_4]^0$ hyperfine matrices, and hyperfine parameters *a*, *b*, *c*

Nucleus	Principal values $\frac{T}{g_e\beta_e}$ (mT)	*a* [a] (mT)	*b* (mT)	*c* (mT)
^1H	0.5473 −0.2291 −0.3182	0.0147	0.2736	0.0451
$^7Li_\alpha$	−0.1246 −0.0485 0.1731	−0.1191	0.0865	0.0381
$^7Li_\beta$	−0.0527 −0.0170 0.0697	−0.0225	0.0348	0.0179

[a] $a = (A_1 + A_2 + A_3)/3g_e\beta_e$
$b = [A_1 - (A_2 + A_3)/2]/3g_e\beta_e$
$c = (|A_2 - A_3|)/2g_e\beta_e$
A_i ($i = 1, 2, 3$) denotes the principal values of A, ordered such that $|A_1 - A_2|$ and $|A_1 - A_3|$ are larger than or equal to $|A_2 - A_3|$, thus selecting A_1, and (arbitrarily) taking $|A_2| - |A_3|$ to be non-negative

electron wavefunction. In the case of an oxygenic hole, the bulk of the spin density is assumed to reside in a 2p orbital of the oxygen atom. The value of $|c_{2p}|^2$ was determined for the aluminum oxygenic hole centre $[AlO_4]^0$ using hyperfine matrices determined for the low-abundance ^{17}O isotope (Nuttall and Weil 1980b). The coefficient is given by the relation

$$|c_{2p}|^2 = \frac{b}{b_0} \quad , \tag{3}$$

where b is the dipolar component of the hyperfine matrix and b_0 is the free-ion hyperfine parameter, discussed by Nuttall and Weil 1980b. The free-ion parameter showed a weak dependence on the charge number assigned to the oxygen atom, which was varied between +1 and −1. Taking the charge number to be + 0.5 gave a value for $|c_{2p}|$ of 0.87. A more negative charge, as suggested by molecular-orbital calculations (Walsby 1999), leads to a slightly larger value.

For $[HLi_2O_4]^0$, distances R were calculated using Eq. (2) with a range in $|c_p|$ of 0.9 ± 0.1, corresponding to an unpaired-electron O_{2p} orbital occupancy ranging from 0.64 to 1.0. A lower value than this would indicate a strongly delocalized system, which is not supported by the g-value analysis described above. Table 4 lists the unique principal directions of the three hyperfine matrices, and the distances calculated using Eq. (2). The resultant positions of the compensators are depicted in Fig. 4.

The uniaxial approximation for the hyperfine matrices implies that the solution for the proton is probably the most reliable . However, the approach provides a useful comparison for the results of the more general analyses subsequently undertaken for all three compensators. Of the two proton-position solutions indicated in Fig. 4, the position associated with O_4 seems more likely. Modelling of the hydrogarnet centre in α-quartz by Purton et al. (1992) placed the protons in positions closely associated with each of the four oxygen atoms surrounding the silicon vacancy, with O–H distances very close to 1.0 Å. The position shown in Fig. 4 is 0.9 Å from O_4.

The second approach taken herein to extract compensator positions from the hyperfine matrices was the use of a more general point-dipole–point-dipole model. This model does not assume a uniaxial hyperfine matrix, and allows both the distance and direction of the compensator M to be fitted. The key equations, taken from Mabbs and Collison (1992) (corrected), are:

$$\begin{aligned}
T_{xx} &= -\frac{\mu_0 g_n \beta_n \beta_e}{4\pi R^3}\left(g_{xx}(1-3l^2) - 3lmg_{yx} - 3lng_{zx}\right) \\
T_{yy} &= -\frac{\mu_0 g_n \beta_n \beta_e}{4\pi R^3}\left(g_{yy}(1-3m^2) - 3lmg_{xy} - 3mng_{zy}\right) \\
T_{zz} &= -\frac{\mu_0 g_n \beta_n \beta_e}{4\pi R^3}\left(g_{zz}(1-3n^2) - 3lng_{xz} - 3mng_{yz}\right) \quad ,
\end{aligned} \tag{4}$$

where T_{xx}, T_{yy} and T_{zz} are the principal values of the dipolar part of the hyperfine matrix, and the g matrix has been transformed into the principal axis system of the hyperfine matrix (by operation of the similarity transformation which diagonalizes $\boldsymbol{A}$). R is the distance O–M. The l, m, n are the direction cosines of the O–M vector in the hyperfine matrix principal axis system, as shown in Fig. 5.

The above equations were written into a program DIPOLE (W.C. Tennant 1999, personal communica-

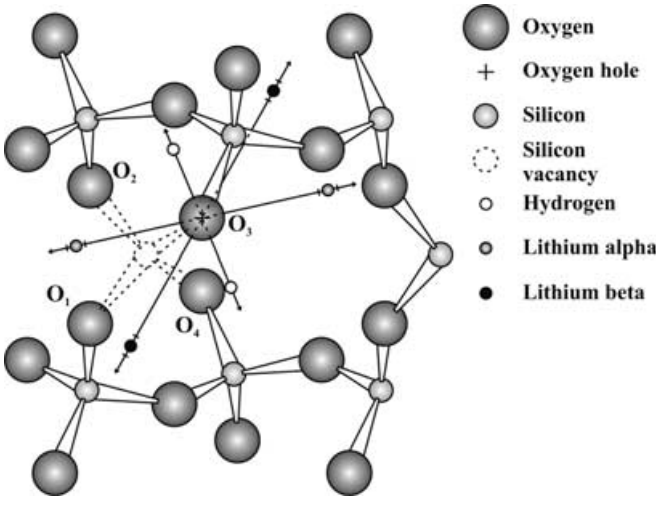

Fig. 4 Calculated positions of the hyperfine nuclei of centre $[HLi_2O_4]^0$ in α-quartz from the magnetic point-dipole – point-dipole model. The *arrows* point in the unique principal directions of the hyperfine matrices used to define the O–M direction in this model. The *perpendicular lines* at either side of the hyperfine nuclei positions represent the error limits due to the choice of $|c_p|$, as discussed in the text. The limits are partially obscured for the proton position by the outline of the atom

Table 4 Distances O–M for centre $[HLi_2O_4]^0$, calculated using Eq. (2), and the unique principal directions (site 1) of the hyperfine matrices. *Numbers in parentheses* indicate equivalent (opposite) directions

M	O–M distance	Unique principal direction	
	(Å)	θ (°)	ϕ (°)
H	2.03 ± 0.15	37.9(142.1)	292.8(112.8)
Li_α	2.17 ± 0.16	82.3(97.7)	12.6(192.6)
Li_β	2.94 ± 0.22	124.0(56.0)	60.7(240.7)

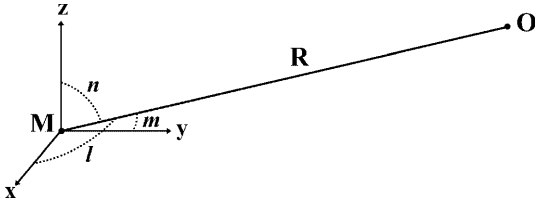

Fig. 5 Model used in program DIPOLE. Direction cosines l, m, n give the direction from the hyperfine nucleus to the oxygen atom in terms of the principal axis system x, y, z of the hyperfine matrix. R is the interatomic distance

tion) which varies the three variables (R and any two of the cosines) until the best agreement with the principal values of the dipolar hyperfine matrix is found. The third direction cosine is given by the requirement that the sum $l^2 + m^2 + n^2$ is equal to 1. The resulting set of direction cosines must then be transformed from the hyperfine principal axis system into the crystal axis system, so that they may be more easily interpreted.

This broader approach yielded multiple "exact" solutions, i.e., sets of fitted variables which all agreed with the experimental principal values within the precision fixed by the program. The various solutions were found by taking different starting values for the variables. Different solutions were also found when the sign of the matrix was changed by multiplying all of the elements by −1. Four independent solutions were found for each of the three hyperfine nuclei, and each of these solutions gave a pair of positions in opposite directions from the oxygen hole. The directions and distances furnished by the solutions obtained for the three hyperfine nuclei using DIPOLE are given in Table 5. Only the exact solutions are included.

The DIPOLE directions and distances in Table 5 may be compared with the directions and point-dipole-calculated distances in Table 4, in order to eliminate those solutions which agree poorly. The closest agreement between the solutions found by the two methods should be better for the proton, due to the greater validity of the uniaxial approximation in this case. This is found to be true. The DIPOLE solution for the proton, $\theta = 14.6°$, $\phi = 304.1°$ is 23.7° away from the unique principal direction of the observed proton hyperfine matrix, and the DIPOLE solution $\theta = 55.9°$, $\phi = 319.5°$ is 26.3° away. The O–H distances are within the range quoted in Table 4. By comparison, the closest agreement for the Li_α solutions is 29.7° for the solution $\theta = 115.8°$, $\phi = 217.4°$, and 32.3° for the solution $\theta = 65.5°$, $\phi = 191.7°$, while the distances are a little outside the range quoted in Table 4. The Li_β solutions show the poorest agreement, the best being $\theta = 25.2°$, $\phi = 199.9°$, 39.4° away from the unique principal direction, with a distance well outside the range quoted in Table 4. These best solutions are depicted in Fig. 6.

Table 5 Polar coordinates of the three hyperfine nuclei, relative to O_3, determined using program DIPOLE. *Numbers in parentheses* indicate equivalent (opposite) directions

Nucleus	Sign[a]	Polar coordinates		R (Å)
		θ (°)	ϕ (°)	
H	+	55.9(124.1)	319.5(139.5)	1.943
		165.4(14.6)	124.1(304.1)	1.989
	−	66.3(113.7)	87.9(267.9)	1.665
		70.4(109.6)	12.2(192.2)	1.687
Li_α	+	114.5(65.5)	11.7(191.7)	1.940
		115.8(64.2)	217.4(37.4)	2.005
	−	101.9(78.1)	285.8(105.8)	1.853
		157.2(22.8)	139.3(319.3)	1.589
Li_β	+	104.3(75.7)	12.9(192.9)	1.815
		154.8(25.2)	19.9(199.9)	2.325
	−	61.1(118.9)	317.1(137.1)	1.877
		118.6(61.4)	254.4(74.4)	1.877

[a] Sign of the "unique" principal value

The two proton positions obtained are environmentally quite different. The position labelled 1 in Fig. 6 is closely associated with O_4, with an O–H distance of 0.94 Å (note that the two-dimensional nature of the figure makes position 1 appear to be closer to O_3). The other position, labelled 2, is located closer to the centre of one of the c-axis channels, and is quite distant from any other atoms. The closest atom is O_4 at a distance of 1.76 Å. The second position is more typical of the M ions of the $[AlO_4/M]^+$ centres (Nuttall and Weil 1981b), but does not agree with the calculations of Purton et al. (1992) for the hydrogarnet defect in α-quartz described earlier. On this basis, the first position seems more likely.

There would initially seem to be no strong reason to prefer either of the two Li_α positions in Fig. 6. However, when the position of the Li_β is taken into account, a possible pattern emerges. Both lithium ions have positions which are very nearly equidistant from two of the oxygen atoms surrounding the vacancy, indicating that they may act as bridging ligands, i.e., analogous to a hydrogen-bond system. Ion Li_α (position 2) appears to bridge between O_1 and O_2, with distances of 1.35 and 1.43 Å, respectively. Ion Li_β bridges between O_2 and O_4, with distances of 1.32 and 1.30 Å, respectively. The Li_β position is, in fact, only 0.03 Å from the tetrahedral edge between the two-oxygen atoms. It should be noted that two-coordinate lithium ions are not usually observed in either organic or inorganic molecules studied by x-ray crystallography (Wozniak and Krygowsky 1993), but may be more likely in a defect system such as studied here, where the lithium ion is not located in a lattice position.

In an effort to help establish these positions more definitely, a third approach was employed to extract the

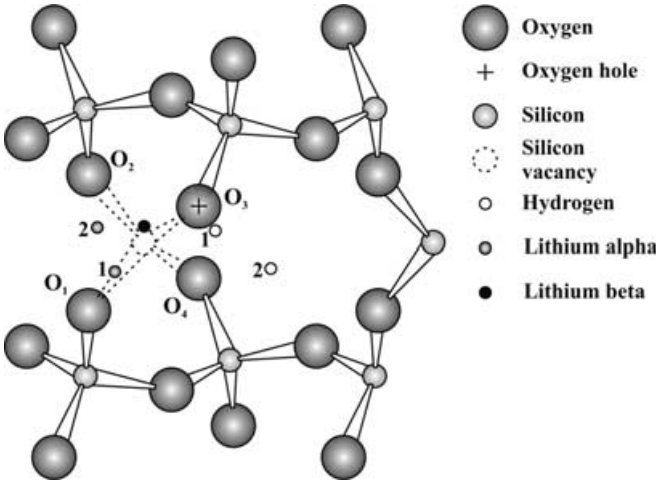

Fig. 6 Best calculated positions for the three hyperfine nuclei of centre $[HLi_2O_4]^0$ in α-quartz, obtained from program DIPOLE, based on agreement with point-dipole – point-dipole analysis. The alternative positions labelled *1* and *2* for both the hydrogen and lithium alpha ions are discussed in the text

hyperfine nuclei positions from the experimental hyperfine matrices. This was achieved through the use of the program FITPKL (Mombourquette 1986; Mombourquette et al. 1995), which calculates dipolar hyperfine matrices using the magnetic interaction between a bare point nucleus, and the electronic spin density in one or more ns and/or np ($n = 2$–4) hydrogenic orbitals centred on one or more atoms. The equations used in the program are based on the work of McConnell and Strathdee (1959) as corrected by Pitzer et al. (1962). They may be found in Mombourquette and Weil (1986) (for $n = 2$, 3), and Dickson et al. (1991) (for $n = 4$). The latter paper also notes a correction to the former.

FITPKL calculates a dipolar hyperfine matrix and minimizes the matrix-element RMSD between the calculated and experimental matrix elements by varying a number of parameters. The varied parameters may include the coordinates of the atom(s) carrying appreciable electronic spin density and the hyperfine nuclei, the effective nuclear charge of the atom(s) carrying the spin density, and the sp admixture of the orbitals involved. The orientation of the p orbital(s) carrying the electronic spin density, the amount of spin density on each atom and the nuclear g value of the hyperfine nucleus are also input, but not varied in the minimization.

All three hyperfine nuclear positions were fitted simultaneously, so that the matrix-element RMSD minimum could be found for all the hyperfine nuclei with the same set of parameters associated with the electronic spin density. The orbital containing this spin density was assumed to be located entirely on the oxygen anion and was initially assumed to arise from a pure p orbital. The orientation of the orbital normally is expected to be perpendicular to the Si–O–Si plane (Nuttall and Weil 1980b, 1981a). However, in the present case, the oxygen anion is adjacent to a silicon vacancy. Orientations of the p orbital kept perpendicular to the remaining Si–O bond were tried over a 180° range in 10° increments, beginning with the usual Si–O–Si perpendicular direction. The effective nuclear-charge number Z of the oxygen nucleus with respect to the unpaired electron was initially taken to be 3.815, calculated using empirical rules (Sakai and Anno 1974). The signs of the hyperfine matrices were taken to be the same as those which had given the most likely positions using DIPOLE, as described above. Choosing any other combination was found to give much poorer fits.

When the best p-orbital orientation was found within the above constraints, the orientation was varied manually without constraint, along with the effective charge, until the lowest RMSD was found. Despite the lack of constraints, the lowest RMSD of 0.0088 mT was found with a p-orbital orientation ($\theta = 35°$, $\phi = 120°$) almost exactly perpendicular to the Si–O bond, making an angle of 89.3°. The value of the oxygen charge number Z was reduced to 2.12, but did not appear to have much effect on the fitted hyperfine nuclei positions. The calculated and experimental matrices are shown for comparison in Table 6, along with the fitted hyperfine nuclei positions.

Table 6 Experimental and calculated matrices $\boldsymbol{T}$ for centre $[HLi_2O_4]^0$, using program FITPKL, and fitted coordinates of the hyperfine nuclei

	Matrix $\frac{\boldsymbol{T}}{g_e\beta_e}$ (mT)			k	Principal value $\frac{T}{g_e\beta_e}$(mT)	Principal direction	
						θ_k (°)	ϕ_k (°)
^{1}H	−0.2323	−0.1459	0.1299	1	0.5473	37.9	292.8
Experimental		−0.0173	−0.3608	2	−0.2291	124.3	321.3
			0.2497	3	−0.3182	76.0	41.5
^{1}H	−0.2383	−0.1232	0.1510	1	0.5467	37.7	293.2
Calculated		−0.0090	−0.3571	2	−0.2546	127.6	298.3
			0.2473	3	−0.2921	87.5	26.4
Coordinates	x	y	z				
	3.5(2)	−0.1(4)	0.75(9)				
Li_α	0.1574	0.0549	0.0242	1	0.1731	82.3	12.6
Experimental		−0.0957	0.0379	2	−0.0485	150.4	296.5
			−0.0616	3	−0.1246	61.6	278.4
Li_α	0.1570	0.0542	0.0273	1	0.1737	81.3	13.0
Calculated		−0.0919	0.0442	2	−0.0461	145.7	295.9
			−0.0651	3	−0.1276	57.1	277.3
Coordinates	x	y	z				
	1.6(6)	0.0(6)	−1.7(1.0)				
Li_β	−0.0183	0.0210	−0.0368	1	0.0697	56.0	240.7
Experimental		0.0270	−0.0399	2	−0.0170	113.7	313.5
			−0.0088	3	−0.0527	136.5	195.9
Li_β	−0.0208	0.0320	−0.0250	1	0.0702	57.9	241.3
Calculated		0.0246	−0.0393	2	−0.0309	137.2	288.6
			−0.0038	3	−0.0393	115.0	168.3
Coordinates	x	y	z				
	2.0(1.0)	−1.3(1.3)	0.6(1.3)				

The best agreement between the experimental and calculated hyperfine matrices was found for the Li_α nucleus. However, the calculation appears to be quite insensitive to the position of the nucleus, as the errors on the fitted coordinates are large. The proton position is fitted more precisely by FITPKL, despite the larger deviation of the experimental matrix from the calculated matrix. The Li_β hyperfine matrix is fitted rather poorly, as reflected in the relatively large errors in the fitted position of the nucleus.

The proton position fitted using FITPKL agrees very well with the preferred DIPOLE solution labelled 1 in Fig. 6, which has the Cartesian coordinates 3.51, 0.19, 0.75 Å, where the origin is at the centre of the large *c*-axis channel on axis $\mathbf{a}_1$. This falls well within the relatively small uncertainty given for the FITPKL solution. The DIPOLE solutions for the position of the Li_α nucleus have the Cartesian coordinates 1.80, −0.49, −2.04 Å (position 1 in Fig. 6), and 1.50, 0.25, −0.36 Å (position 2 of Fig. 6). The first position agrees best with the FITPKL solution in terms of an RMSD, due to the poor agreement of the *z* coordinate of the second position, which lies outside the quoted uncertainty of the FITPKL solution. However, the *z* coordinate clearly is poorly fitted by FITPKL, so this may have little meaning. The other two coordinates of position 2 are closer than the corresponding coordinates of position 1. Position 2 is the bridging position discussed earlier, which appears the more likely structure. The DIPOLE solution for the position of Li_β (2.30, 0.27, 0.93 Å) also agrees with the FITPKL solution within the quoted uncertainties for two of the coordinates, *x* and *z*, but not for the *y* coordinate. However, the FITPKL coordinates are quite poorly fitted for Li_β.

No improvement was found in the RMSD when *s* character was introduced into the electronic wavefunction, or when part of the electronic spin density was placed on other nearby atoms. Finally, a fit was made for each of the three hyperfine nuclei independently, where all of the parameters were allowed to vary simply to obtain the best fit. In this way, hyperfine matrices were calculated which agreed exactly with the experimental matrices within their uncertainties. Because the three matrices were fitted independently, the *p*-orbital orientations for each calculation were significantly different, which cannot be a true reflection of the physical case. However, it is interesting to note the positions calculated in this way, which are determined very precisely. The differences in the positions from the combined and independent calculations are not great, with almost all of the coordinates from the independent calculation within the uncertainties given for the combined calculation in Table 6. Most noteworthy is that the single poorly agreeing coordinate discussed earlier for both of the lithium nuclei becomes significantly closer to the preferred DIPOLE coordinate in both cases. In particular, the second Li_α (bridging) position from DIPOLE discussed above is in better agreement with the independent FITPKL position than the first DIPOLE Li_α position.

The combination of the three techniques for fitting the hyperfine nuclei positions yields a set of positions which is not unreasonable. The proton position can be assigned with reasonable confidence, given supporting evidence provided by all three techniques. It appears that the proton is closely associated with O_4, adjacent to the main *c*-axis channel, with an O–H bond distance probably of the order of 1 Å. While the lithium nuclei may not be assigned with as much confidence, the calculations suggest positions roughly equidistant from two oxygen anions surrounding the silicon vacancy, close to the tetrahedral edges formed by the four anions. For Li_α, it is the O_1–O_2 edge, and for Li_β, the O_2–O_4 edge. None of the nuclei is shown to be associated with the oxygen anion bearing the hole, in agreement with the suggested structure of the $[H_3O_4]^0$ centre (Nuttall and Weil 1980a). The three suggested positions relative to the oxygen tetrahedron surrounding the vacancy are shown in Fig. 7.

The feasibility of our model, especially the electronic structure and the nature of the bonding, needs to be tested by more sophisticated quantum-mechanical modelling. It has been assumed up to this point that the charge number of the compensator ions is exactly +1. This is clearly not the case, as all three hyperfine matrices have an isotropic component (Table 3), indicative of some degree of spin density located on the ions. The isotropic part of the hyperfine interaction has been neglected in the modelling studies described herein, which did not take any value of the ionic charge into account. It is not yet clear how the Li nuclei are bound within the site, nor how the normal distribution of electrons in the quartz SiO_4 units is affected by the silicon vacancy. All of the hyperfine ions appear to be locked in position, as shown by the narrowness of the lines in the EPR spectrum, the well-defined hyperfine matrices and the stability of the centre towards high-temperature annealing.

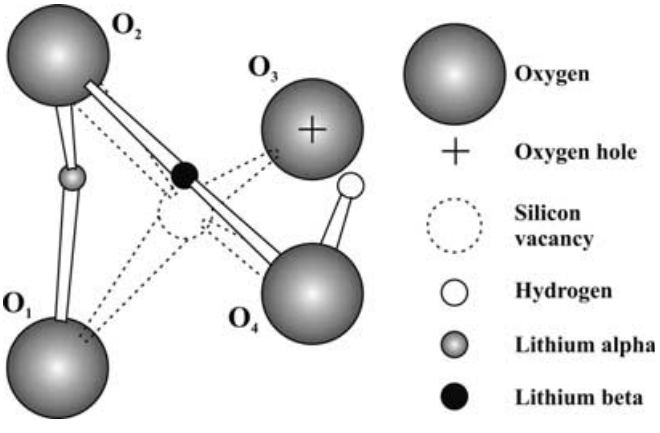

Fig. 7 Final postulated positions for the three hyperfine nuclei of centre $[HLi_2O_4]^0$ in α-quartz, based on the three analyses described in the text. Only the four oxygen atoms of the approximate tetrahedron surrounding the silicon vacancy are shown. The orientation is the same as in the previous diagrams

The silicon vacancy/oxygen hole model for $[HLi_2O_4]^0$ also poses the question of why no other of the conceivable analogues has been observed, and what the nature of the defect might be before irradiation. Given that Li^+ and H^+ are present in the crystal, there seems no obvious reason why other combinations, such as $[H_2LiO_4]^0$ or $[Li_3O_4]^0$, would not be possible. The apparent absence of the first of these is particularly surprising in light of the concurrent observation of $[FeO_4/H]^0$ (Mombourquette et al. 1989) and not $[FeO_4/Li]^0$ (Halliburton et al. 1989) in this crystal, suggesting higher concentrations of protons than lithium ions in this crystal. While there exist some as yet unidentified signals in the EPR spectra of the crystal, they are very weak, and any other species are clearly present at a considerably lower concentration than $[HLi_2O_4]^0$.

It is possible that the hydrogarnet-related species which have been observed are simply more stable than the other putative species. The paramagnetic $[H_3O_4]^0$ centre is thought to be formed from the paramagnetic $[H_4O_4]^+$ centre by the loss of a proton to form a stable neutral species. $[H_4O_4]^+$ in turn is thought to be formed from the diamagnetic hydrogarnet defect $[H_4O_4]^0$. Similar precursors might exist for $[HLi_2O_4]^0$ also. Any possible combination of four H^+ or Li^+ ions in a diamagnetic hydrogarnet-type precursor other than $4Li^+$ could potentially lead to one of the two observed neutral paramagnetic centres, $[HLi_2O_4]^0$ and $[H_3O_4]^0$. This is shown in Fig. 8. The diamagnetic species on the left may become paramagnetic oxygenic hole centres following irradiation, and then form neutral paramagnetic species, as on the right, by the loss of a proton (horizontal path) or lithium ion (diagonal path). One might also envisage the loss of a neutral proton or lithium atom, which would give the same results as shown in Fig. 8 in a one-step process. Lithium atoms are known in α-quartz (Wilson et al. 1986), and are thought to be involved in the initial stage of the $[AlO_4/Li]^q$ centre (Walsby et al. 2003), observed in crystals cut from the same plate. If the two final products shown in bold in Fig. 8 are more stable, then the pathways which lead to the formation of these centres may be dominant. Further experiments involving EPR analysis immediately following gamma irradiation at low temperature may determine if there are any four +1 ion-compensated centres other than $[H_4O_4]^+$. The observation of a paramagnetic precursor to the $[HLi_2O_4]^0$ centre would go a long way towards confirming the suggested silicon vacancy/oxygenic hole model.

There is another known centre in quartz which contains two lithium cations and a single hydrogen ion, but it has a quite different structure. This is the Ge^{3+} centre $[GeO_4/HLi_2]^0$ (Weil 1971). This centre is thought to arise from a diamagnetic precursor $[GeO_4/Li_2]^0$ with Ge^{2+} substituted for Si^{4+} within an oxygen tetrahedron, and two Li^+ compensators occurring nearby in opposite-side *c*-axis channels. Upon irradiation of the crystal at room temperature, hydrogen atoms are formed elsewhere, diffuse readily through the crystal at this temperature, and react with the Ge^{2+} ion to yield Ge^{3+} and an attached hydride ion, H^-, via electron transfer. However, there is no evidence for the presence of germanium in the present crystal studied, and no likely alternative species seem possible which can exist in a stable + 2 or + 3 oxidation state, which have no $I \neq 0$ isotopes of appreciable abundance, and which could substitute for silicon in the quartz lattice. Furthermore, the two Li^+ ions are not nearly equivalent here, as is the case for $GeHLi_2$. Also, the ^1H hyperfine interaction here is much smaller, and the *g*-matrix principal directions do not have the same strong correlation with those of $[HLi_2O_4]^0$, as shown by the aluminum and hydrogenic defects discussed earlier.

The silicon vacancy/oxygen hole model for the centre reported here appears to fit best with the experimental data. The confirmed existence of an analogue to the hydrogarnet defect which does not contain only protons could be of some significance to the topic discussed in the introductory section. While the hydrogarnet defect is deemed to produce quartz and molecular water upon heating, a centre containing a mixture of hydrogen and lithium ions would presumably behave differently, perhaps lessening the hydrolytic weakening effect when it replaces the hydrogen-type hydrogarnet defects.

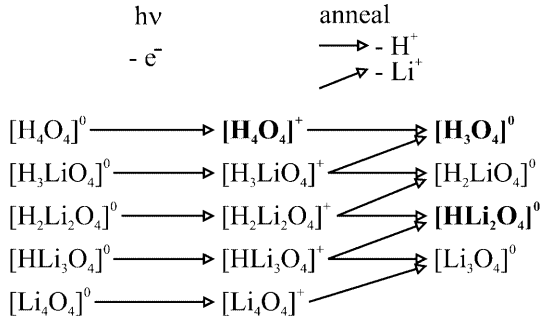

Fig. 8 Representation of the precursor (diamagnetic) hydrogarnet-type defects with H^+ and Li^+ compensators only, and some possible paths to produce various paramagnetic centres. Those of the latter which have been observed by EPR are shown in *bold*

Acknowledgements We gratefully acknowledge the continued co-operation and interest of Sawyer Research Products Inc., who furnished the quartz crystal utilized. We are especially indebted to Dr. W.C. Tennant for much advice and discussion during the course of this work. This work was carried out with resources provided by the NZ Universities Grants Committee and the Department of Chemistry, University of Canterbury. We also acknowledge partial support from the Natural Sciences and Research Council of Canada.

References

Abragam A, Bleaney B (1970) Electron paramagnetic resonance of transition ions. Clarendon Press, Oxford, UK

Claridge RFC, Mackle KM, Sutton GLA, Tennant WC (1994) Zircon EPR revisited: 10 K EPR of three low-symmetry centres in irradiated zircon (zircon silicate). J Phys Condens Matter 6:3429–3436

Cordier P, Doukhan JC (1989) Water solubility in quartz and its influence on ductility. Eur J Mineral 1:221–237

Cordier P, Weil JA, Howarth DF, Doukhan JC (1994) Influence of the $(4H)_{Si}$ defect on dislocation motion in crystalline quartz. Eur J Mineral 6:17–22

Dickson RS, Weil JA (1990) The magnetic properties of the oxygen-hole aluminum centres in crystalline SiO_2. IV. $[AlO_4/Na]^+$. Can J Phys 68:630–642

Dickson RS, Weil JA, Davis PH (1991) The paramagnetic germanium–sodium impurity centres $[GeO_4/Na]^0_A$ and $[GeO_4/Na]^0_C$ in α-quartz. Can J Phys 69: 761–779

Halliburton LE, Hantehzadeh MR, Minge J, Mombourquette MJ, Weil JA (1989) EPR study of Fe^{3+} in α-quartz: a reexamination of the lithium-compensated center. Phys Rev(B) 40:2076–2081

Lin JS, Payne MC, Heine V, McConnell JDC (1994) Ab initio calculations on $(OH)_4$ defects in α-quartz. Phys Chem Miner 21:150–155

Mabbs FE, Collison D (1992) Electron paramagnetic resonance of *d* transition metal compounds. Elsevier, Amsterdam, The Netherlands

McConnell HM, Strathdee J (1959) Theory of anisotropic hyperfine interactions in π-electron radicals. J Mol Phys 2:129–138

McConnell JDC, Lin JS, Heine V (1995) The solubility of $[4H]_{Si}$ defects in α-quartz and their role in the formation of molecular water and related weakening on heating. Phys Chem Miner 22:357–366

McLaren AC, Cook RF, Hyde ST, Tobin RC (1983) The mechanisms of formation and growth of water bubbles and associated dislocation loops in synthetic quartz . Phys Chem Miner 9:79–94

McLaren AC, FitzGerald JD, Gerretsen J (1989) Dislocation nucleation and multiplication in synthetic quartz: relevance to water weakening. Phys Chem Miner 16:465–482

Mombourquette MJ (1986) Program MSPKL.FOR. PhD Thesis, University of Saskatchewan, Saskatoon, Canada

Mombourquette MJ, Weil JA (1985) Ab initio self-consistent-field molecular-orbital calculations on AlO_4 centres in alpha-quartz. II. Can J Phys 63:1282–1293

Mombourquette MJ, Weil JA (1986) Structure determination of the AlO_4 hole centres in α-quartz by EPR and SCF MO. J Magn Reson 66:105–117

Mombourquette MJ, Weil JA, Mezey PG (1984) Ab initio SCF MO calculations on AlO_4 centres in alpha-quartz. I. Can J Phys 62:21–34

Mombourquette MJ, Minge J, Hantehzadeh MR, Weil JA, Halliburton LE (1989) Electron paramagnetic resonance study of Fe^{3+} in α-quartz: hydrogen-compensated center. Phys Rev(B) 39:4004–4008

Mombourquette MJ, McEachern RJ, Weil JA (1995) Atom positions from hyperfine data for germanium centers in α-quartz. Magn Reson Chem 33:S70–S80

Mombourquette MJ, Weil JA, McGavin DG (1996) Computer program EPR–NMR. Department of Chemistry, University of Saskatchewan, Canada. Available from one (J.A.W.) of the authors.

Nobes RH, Akhmatskaya EV, White JA, Winkler B, Pickard CJ (2000) An ab initio study of hydrogarnets. Am Mineral 85:1706–1715

Nuttall RHD, Weil JA (1980a) Two hydrogenic trapped-hole species in α-quartz. Solid State Commun 33:99–102

Nuttall RHD, Weil JA (1980b) Oxygen-17 hyperfine structure of trapped-hole center $[AlO_4]^0$ in α-quartz. Solid State Commun 35:789–791

Nuttall RHD, Weil JA (1981a) The magnetic properties of the oxygen-hole aluminum centres in crystalline SiO_2. I. $[AlO_4]^0$. Can J Phys 59:1696–1708

Nuttall RHD, Weil JA (1981b) The magnetic properties of the oxygen-hole aluminum centres in crystalline SiO_2. II. $[AlO_4/H]^+$ and $[AlO_4/Li]^+$. Can J Phys 59:1709–1718

Nuttall RHD, Weil JA (1981c) The magnetic properties of the oxygen-hole aluminum centres in crystalline SiO_2. III. $[AlO_4]^+$. Can J Phys 59:1886–1892

Paterson MS (1986) The thermodynamics of water in quartz. Phys Chem Miner 13:245–255

Perlson BD, Weil JA (1975) Variable low-temperature EPR cavity. Rev Sci Instrum 46: 874–878

Pitzer RM, Kern CW, Lipscomb WN (1962) Evaluation of molecular integrals by solid spherical harmonic expansions. J Chem Phys 37:267–274

Purton J, Jones R, Heggie M, Öberg S, Catlow CRA (1992) LDF pseudopotential calculations of the α-quartz structure and hydrogarnet defect. Phys Chem Miner 18:389–392

Sakai Y, Anno T (1974) New set of rules of the Slater type on the screening constants and the effective principal quantum numbers. J Chem Phys 60:620–624

Walsby CJ (1999) Theoretical and experimental electron paramagnetic resonance studies of single crystals. PhD dissertation. University of Canterbury, Christchurch, New Zealand

Walsby CJ, Lees NS, Claridge RFC, Weil JA (2003) The magnetic properties of oxygen-hole aluminum centres in crystalline SiO_2. VI. A stable AlO_4/Li centre. Can J Phys, accepted.

Weber RT (1995) WIN-EPR SimFonia user's manual (software version 1.2). EPR Division, Bruker Instruments, Inc., Billerica, MA, USA

Weil JA (1971) Germanium–hydrogen–lithium center in α–quartz. J Chem Phys 55:4685–4698

Weil JA (1975) Comments on second-order spin-Hamiltonian energies. J Magn Reson 18:113–116

Weil JA, Anderson JH (1961) Direct field effects in electron paramagnetic resonance hyperfine spectra. J Chem Phys 35:1410–1417

Weil JA, Buch T, Clapp JE (1973) Crystal point-group symmetry and microscopic tensor properties in magnetic resonance spectroscopy. Adv Magn Reson 6:183–256

Weil JA, Bolton JR, Wertz JE (1994) Electron paramagnetic resonance: elementary theory and practical applications. Wiley, New York, USA

Wilson TM, Weil JA, Rao PS (1986) Electronic structure of the interstitial lithium-associated electron trap in crystalline quartz. Phys Rev(B) 34:6053–6055

Wozniak K, Krygowski TM (1993) Structural features of lithium–oxygen bond retrieved for ionic crystals from Cambridge structural database and inorganic structural database. Pol J Chem 67:1667–1674

Wyckoff RWG (1963) Crystal structures, 2nd ed, vol 1. Interscience, New York, USA